Inorganic Chemistry

Article

pubs.acs.org/IC

Synthesis and Structure Resolution of $RbLaF_4$

Anne-Laure Rollet,*[,§] Mathieu Allix,[†,‡] Emmanuel Veron,[†,‡] Michael Deschamps,[†,‡] Valérie Montouillout,[†,‡] Matthew R. Suchomel,[∥] Emmanuelle Suard,[⊥] Maud Barre,[#] Manuel Ocaña,[∇] Aymeric Sadoc,[○] Florent Boucher,[○] Catherine Bessada,[†,‡] Dominique Massiot,[†,‡] and Franck Fayon[†,‡]

[†]CEMHTI, CNRS UPR 3079, Orléans, France

[‡]Université d'Orléans, Faculté des Sciences, Orléans, France

[§]PECSA, CNRS, UPMC Univ Paris 06, ESPCI UMR 7195, Paris, France

[∥]Argonne National Laboratory, Advanced Photon Source, Argonne, Illinois 60439, United States

[⊥]Institut Max Von Laue Paul Langevin, Grenoble, France

[#]Laboratoire des Oxydes et Fluorures, Université du Maine, CNRS UMR 6010, Le Mans, France

[∇]Instituto de Ciencia de Materiales de Sevilla, CSIC-US, Sevilla, Spain

[○]Institut des Matériaux Jean Rouxel (IMN), Université de Nantes, CNRS UMR 6502, Nantes, France

Supporting Information

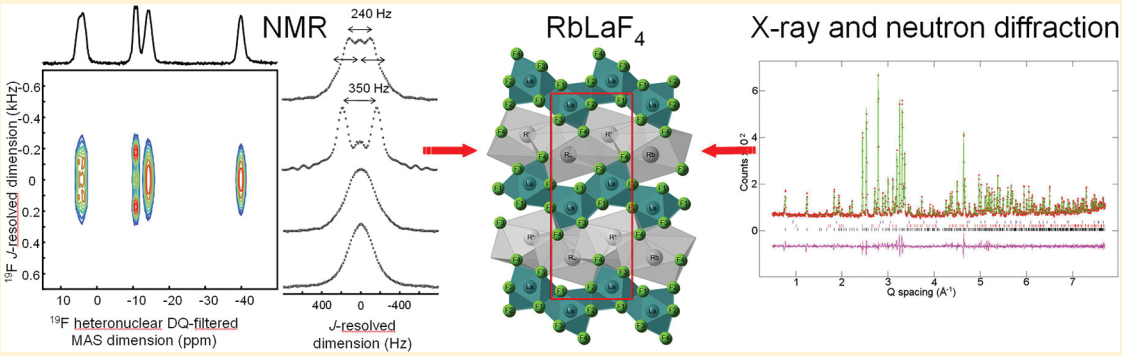

ABSTRACT: The synthesis and structure resolution of $RbLaF_4$ are described. $RbLaF_4$ is synthesized by solid-state reaction between RbF and LaF_3 at 425 °C under a nonoxidizing atmosphere. Its crystal structure has been resolved by combining neutron and synchrotron powder diffraction data refinements (*Pnma*, a = 6.46281(2) Å, b = 3.86498(1) Å, c = 16.17629(4) Å, Z = 4). One-dimensional ^{87}Rb, ^{139}La, and ^{19}F MAS NMR spectra have been recorded and are in agreement with the proposed structural model. Assignment of the ^{19}F resonances is performed on the basis of both ^{19}F−^{139}La *J*-coupling multiplet patterns observed in a heteronuclear DQ-filtered *J*-resolved spectrum and ^{19}F−^{87}Rb HMQC MAS experiments. DFT calculations of both the ^{19}F isotropic chemical shieldings and the ^{87}Rb, ^{139}La electric field gradient tensors using the GIPAW and PAW methods implemented in the CASTEP code are in good agreement with the experimental values and support the proposed structural model. Finally, the conductivity of $RbLaF_4$ and luminescence properties of Eu-doped $LaRbF_4$ are investigated.

INTRODUCTION

Rare-earth fluorides have generated considerable interest as promising materials for many applications, such as solid electrolyte and optical material, as well as in the field of future nuclear energy technologies. Due to their high fluorine-ion conductivity and moderate electronic conductivity, rare-earth fluoride compounds are good candidates for use as solid electrolytes in electrochemical sensors. Most of these compounds belong to the MF_2−RF_3 binary systems with M = Ca, Sr, Ba, Cd, Pb and R = Sc, Y, La Lu and usually adopt the fluorite- or tysonite-type structures. The high ionic conductivity values of these compounds (up to 10^{-1}S/cm) have motivated numerous investigations of the relationship between ionic mobility and crystallographic structure, and it has been shown that the superionicity is related to deviations from the ideal stoichiometry occurring when ions with different valences are isostructurally exchanged in the structure.[1] The optical response of these materials is also appealing, and several fluoride salts doped with rare earths (Ce, Gd, Nd, Eu) have been examined for use in UV and VUV lasers[2] or as phosphors in fluorescence lamps.[3,4] For such applications, fluorides exhibit attractive properties: first, they can combine transparency over the infrared to the UV spectrum with low phonon energies that prevent important nonradiative relaxation; second, the UV beam is directly produced by $4f^{n-1}5d \rightarrow 4f^n$ transitions of the

Received: October 24, 2011
Published: February 8, 2012

rare-earth dopant; third, the numerous vibronic transitions make it possible to build tunable lasers. The synthesis of new fluoride compounds (both crystalline and glasses) and investigation of the relationship between their structures and their luminescence properties were described in numerous reports.[5−8]

Molten rare-earth fluorides have also received attention in recent years because of their potential applications in pyrochemical treatment of nuclear wastes, i.e., dissolution of spent fuel in a mixture of alkali fluorides, allowing selective extraction of radionuclides by electrochemical reduction.[9,10] In addition, rare-earth fluorides are of interest in the field of molten salt nuclear reactors (MSR) which are still considered as a potentially cleaner and safer reactor for the future.[11,12] In MSR reactors, the fuel is composed of molten ThF_4−LiF that acts also as coolant. In principle, this technology will allow more easily and continuously to remove the fuel from the core and to recycle it while running. Nevertheless, many technological challenges have to be overcome before the industrial stage, and among them the behavior and effect of rare-earth fission products in the MSR circuit have to be addressed. Therefore, the physical and chemical properties of various molten fluoride mixtures have to be known over a wide range of concentration, temperature, and pressure. To obtain information about the speciation of rare earths in molten fluorides, in-situ NMR[13,14] and EXAFS[15−17] spectroscopies have already been successfully employed. However, interpretation of the spectra obtained using these techniques is partly based on the comparison with crystalline reference compounds of similar composition.[18] Therefore, an extended knowledge of the structures of $A_xR_yF_z$ compounds is highly desirable. This current study was motivated by the need of additional structural data on solid rare-earth fluorides to be compared to the corresponding high-temperature liquids.[19] The phase diagrams of LaF_3−LiF, LaF_3−NaF, LaF_3−KF, LaF_3−RbF, and LaF_3−CsF have been reported, and several $A_xR_yF_z$ compounds have been identified:[20−22] $NaLaF_4$, $KLaF_4$, K_3LaF_6, Rb_3LaF_6, Rb_2LaF_5, $RbLaF_4$, $RbLa_2F_7$, and Cs_3LaF_6. Among these, only the structures of $NaLaF_4$ and $KLaF_4$ have been determined. $NaLaF_4$ crystallizes in the hexagonal $P\bar{6}$ space group,[23] and $KLaF_4$[24] crystallizes in the cubic $Fm\bar{3}m$ space group where K^+ and La^{3+} ions randomly occupy the cationic sites. Despite not being reported in the published phase diagrams, KLa_2F_7 was disclosed by Schmutz[25] and its structure resolved by Pierrard et al.[5] Similarly to $KLaF_4$, it crystallizes in the cubic $Fm\bar{3}m$ space group. It is worth noting that $NaLaF_4$ and $KLaF_4$ are promising phosphor materials when doped.[26,27]

This work focuses on the $Rb_xLa_yF_z$ system and describes the synthesis and structure resolution of $RbLaF_4$ using the combination of both neutron and synchrotron powder diffraction. The number of crystallographically inequivalent cationic and anionic sites is also probed using multinuclear solid-state NMR, and DFT calculations of the ^{19}F isotropic chemical shieldings and of the ^{87}Rb, ^{139}La electric field gradient tensors using the GIPAW and PAW methods are compared to the experimental values. The conductivity and luminescence properties of Eu-doped of $RbLaF_4$ are also investigated.

■ EXPERIMENTAL SECTION

Synthesis. $RbLaF_4$ was synthesized by solid-state reaction using LaF_3 (99.99%, Alfa Aesar) and RbF (99.975%, Alfa Aesar) as starting materials in a 1:1 stoichiometric ratio. The highly hygroscopic RbF salt was dried overnight at 120 °C under vacuum before use, and the mixture was prepared in a glovebox under an argon atmosphere to avoid moisture and oxygen contamination. The optimal heating temperature to obtain pure $RbLaF_4$ was determined from in-situ high-temperature X-ray diffraction experiments from room temperature to 750 °C following the LaF_3−RbF phase diagram.[28] The evolution of the diffractograms as a function of heating temperature indicates that $RbLaF_4$ is formed at 400 °C (Figure S1, Supporting Information). It should be mentioned that extra peaks are observed in addition to the previously reported JCPDF 00-010-0142 indexation. The optimal heating temperature was established as 425 °C, and after prolonged heating for 2 days at this temperature with one regrinding step high-purity $RbLaF_4$ can be obtained (less than 0.5 wt % of LaF_3 remaining impurity). $RbLaF_4$ is stable at room temperature and under ambient atmosphere and is not sensitive to moisture for several months.

A larger amount of sample (5 g) was synthesized for the neutron powder diffraction experiment. A boron nitride crucible without any oxide binder (AX05 grade) filled with the starting materials was heated at 425 °C for $_{two}$ days in a tubular furnace under argon stream. This protocol was repeated three times with regrinding steps at each cycle, and reaction progress was monitored by ex-situ room-temperature XRD.

X-ray, Synchrotron, and Neutron Powder Diffraction. In-situ high-temperature X-ray diffraction (XRD) has been performed on a Bruker AXS D8 diffractometer (θ−θ Bragg−Brentano configuration, Cu Kα radiation, Linear Vantec-1 detector) equipped with an HTK1200N furnace chamber. A pellet (0.8 mm thick, 16 mm diameter) of mixed starting materials has been prepared and loaded inside a boron nitride (BN) crucible, which was subsequently introduced in the furnace chamber swept by a nitrogen flow (0.5 L/min) in order to prevent the sample from oxidizing during the experiment.

High-intensity and high-resolution synchrotron powder XRD data have been recorded on the 11-BM diffractometer at the Advanced Photon Source (APS), Argonne National Laboratory. Data were collected over the 0.5−50° 2θ range with a 0.001° step size at room temperature using a wavelength of λ = 0.412213 Å. The sample was contained in a 0.5 mm capillary and spun at 600 Hz during data collection.

The room-temperature neutron powder diffraction (NPD) pattern of $RbLaF_4$ was collected on the D2B high-resolution/high-flux powder diffractometer at the Institut Laüe-Langevin in Grenoble, France. The sample was packed in a vanadium can. Data were acquired with λ = 1.59432 Å at 2θ intervals of 0.05° over the 10° < 2θ < 160° angular range.

The ICDD JCPDF database[29] was used for identification of observed phases in the XRD and NPD patterns. Rietveld analysis of XRD and NPD data was carried out using the GSAS software package[30] with the EXPGUI interface.[31]

Solid-State NMR. ^{19}F, ^{87}Rb, and ^{139}La solid-state nuclear magnetic resonance (NMR) experiments were carried out at room temperature on Bruker Avance III WB 750 MHz and WB 850 MHz spectrometers operating at magnetic fields of 17.6 and 19.9 T, respectively, using 2.5 mm double-resonance (^{139}La at 17.6 T), 1.3 mm double-resonance (^{19}F and ^{87}Rb at 17.6 T), and 1.3 mm triple resonance (^{19}F, ^{87}Rb and ^{139}La at 19.9 T) MAS Bruker probeheads.

^{87}Rb and ^{139}La central transition (CT) magic angle spinning (MAS) NMR spectra were recorded at 17.6 and 19.9 T using a rotor-synchronized Hahn echo sequence with acquisition at the top of the echo (echo delay set to one rotor period). The ^{87}Rb and ^{139}La CT static spectra were recorded at 17.6 and 19.9 T using a Hahn echo sequence with acquisition of the full echo. The processing of top-echo or full-echo data sets allows obtaining pure phase spectra with flat baselines. The durations of the ^{87}Rb CT-selective 90° pulses were 2.0 (17.6 T) and 1.1 μs (19.9 T), and the durations of the ^{139}La CT-selective 90° pulses were 2.2 (17.6 T) and 1.1 μs (19.9 T). For ^{87}Rb and ^{139}La experiments, the recycle delay was set to 1 s. ^{19}F XiX decoupling[32] with a pulse length of 2.85 τ_R and continuous wave (CW) decoupling sequences were applied during acquisition of MAS and static spectra, respectively. The corresponding ^{19}F nutation frequencies were 89 (17.6 T) and 156 kHz (19.9 T).

The ^{19}F quantitative one-dimensional 1D MAS spectra were recorded at 17.6 and 19.9 T using a 90° flip angle (^{19}F nutation frequency of 140 kHz) and a recycle delay of 2000 s. Since these MAS spectra exhibit spinning sidebands even at high spinning frequencies (66 kHz), the equivalent *infinite spinning rate* ^{19}F spectra were reconstructed from the two-dimensional one pulse[33] (TOP) processing.[34]

The two-dimensional (2D) $^{19}F-^{139}La$ heteronuclear double-quantum (DQ) filtered *J*-resolved spectrum[35] was recorded at 19.9 T with a spinning frequency of 65 kHz. For the heteronuclear DQ filter, rotor-synchronized delays of 0.860 ms and ^{139}La CT-selective 90° pulse lengths of 1.1 μs were used. In the *J*-resolved block, the duration of ^{19}F and ^{139}La (CT) refocusing pulses was 2.6 and 2.2 μs. Presaturation loops and a recycle delay of 120 s were employed. Twenty-two rotor-synchronized t_1 increments of 277 μs with 32 scans each were collected.

The 1D $^{19}F-^{87}Rb$ HMQC MAS experiment[36−38] was performed at 17.6 T with a spinning frequency of 66 kHz. The ^{87}Rb CT-selective 90° pulse length was 4.0 μs, and the ^{19}F 90° pulse length was 1.77 μs. The rotor-synchronized delay for excitation and reconversion of heteronuclear DQ coherences was set to 1.135 ms. Presaturation loops and a recycle delay of 200 s were used, and 64 transients were coadded.

The 2D ^{19}F homonuclear double-quantum single-quantum (DQ-SQ) MAS correlation spectrum was recorded at 17.6 T and 66 kHz spinning rate using the DH^3 experiment.[39] The rotor-synchronized DQ excitation and reconversion periods were both set to 1.060 ms. Presaturation loops and a recycle delay of 80 s were employed. Thirty two t_1 increments of 15.1 μs (i.e., one rotor period) with 16 scans each were collected.

^{87}Rb, ^{139}La, and ^{19}F chemical shifts were referenced relative to 0.01 M aqueous RbCl and 1.0 M aqueous $LaCl_3$ and $CFCl_3$ solutions.[40] All spectra were fitted using the DMfit software.[41] Simulated lineshapes shown in Figure S5b, Supporting Information, were computed using the WSolids1 software.[42]

DFT Calculations. DFT calculations of the NMR parameters were performed with the CASTEP[43,44] code implemented in the Materials Studio 5.0 environment using the projector-augmented waves (PAW)[45] and gauge-included projector augmented waves (GIPAW)[46] algorithms for computing the EFGs and NMR chemical shieldings, respectively. The Perdew−Burke−Ernzerhof (PBE)[47] functional was used for the exchange-correlation kernel. The core−valence interactions were described by ultrasoft pseudopotentials (USPP).[48] The USPP were generated using the on the fly generator (OTF_USPP) included in CASTEP. For fluorine, a core radius of 1.4 Å was used with 2s and 2p valence orbitals; for rubidium, a core radius of 2.5 Å was used with 4s, 4p, and 5s valence orbitals; for lanthanum, a core radius of 2.0 Å was used with 5s, 5p, 4f, 6s, and 5d valence orbitals. As recently described,[49] the local potential of La^{3+} ($4f^0$) USPP was shifted higher in energy (4f shift of 4.55 eV) relative to the default definition of the Materials Studio package. This allows overcoming the deficiency of the PBE exchange-correlation functional which generates in the present case too much covalency between the lanthanum 4f empty states and the anionic fluorine 2p levels.[49] As shown in ref 49, this adaptation of the lanthanum USPP is required to obtain correct values of the ^{19}F shielding parameters when fluorine atoms are bonded to lanthanum. An energy cutoff of 700 eV is used for the plane wave basis set expansion, and the Brillouin zone was sampled using a Monkhorst-Pack grid spacing of 0.04 $Å^{-1}$ (corresponding to a *k*-point mesh of 4 × 6 × 2). Computations of the NMR parameters were performed for both the experimental and the atomic position optimized (APO) structures of $RbLaF_4$. The APO structure was obtained by minimizing the residual forces on all atoms up to $|F|_{max}$ below 6 meV·$Å^{-1}$, keeping symmetry constraints and fixing the cell parameters to the experimentally determined values.

Conductivity Measurement. Electrical conductivity measurements were performed on $RbLaF_4$ pellets sintered at 425 °C (diameter ≈ 5 mm, thickness ≈ 1.5 mm, and compaction around 90%). Thin platinum films were deposited on each face of the pellets by radiofrequency sputtering using a Sputter Coater Polaron SC7620 apparatus. The impedance spectra were recorded over the frequency range from 10 MHz to 0.1 Hz (10 cycles, 20 points/decade) every 40 °C from 147 to 387 °C (on both sample heating and cooling) under dry nitrogen flow using a Schlumberger Solartron 1260 frequency response analyzer connected to a Schlumberger Solartron 1296 dielectric interface. An ac voltage of 50 mV was used, and a waiting time of 20 min was necessary to reach thermal equilibrium after each 40 °C heating or cooling step. Data were analyzed using the Z-view 3.3a software.[50]

Luminescence of Eu-Doped $RbLaF_4$. Excitation and emission spectra of the 5%Eu-doped $RbLaF_4$ ($RbLa_{0.95}Eu_{0.05}F_4$) pellets were recorded in a Horiba Jobin-Yvon Fluorolog spectrofluorometer. The photographs showing the luminescence of the nanophosphor powders deposited on Millipore filters were taken under illumination with ultraviolet radiation (λ = 254 nm), filtered from a Hg discharge lamp.

■ RESULTS AND DISCUSSION

Structural Model Resolution of $RbLaF_4$ from Synchrotron and Neutron Powder Diffraction Data Refinements. As already mentioned, no structural model or cell parameters have been reported to date for $RbLaF_4$. Therefore, an autoindexing analysis of the room-temperature X-ray powder diffraction (XRPD) pattern of $RbLaF_4$ was performed first. Both the Dicvol[51] and Treor[52] indexing routines lead to the same solution with good reliability factors: an orthorhombic cell with *a* = 6.46 Å, *b* = 3.86 Å, and *c* = 16.16 Å. A subsequent ICDD database search using similar cell parameters and chemistry restrictions (only alkali metals, lanthanides, and fluorine) allows finding three compounds with similar indexation: $KCeF_4$ (ICSD 23229; PDF 01-073-0797),[53] $KSmF_4$ (ICSD 20051; PDF 01-072-1816),[54] and $KPrF_4$ (ICSD 281289; PDF 01-071-2541).[55] These three compounds crystallize in the *Pnma* space group symmetry. With $RbLaF_4$ being not stable under an electron beam (amorphization immediately occurs), an electron diffraction study did not allow us to confirm this space group. The proposed *Pnma* orthorhombic indexation was then tested performing a Lebail fit of the XRPD pattern, and the obtained good reliability factors likely confirm the similarity with the $KCeF_4$-type structure.

In order to determine precisely the structure of $RbLaF_4$, a combined Rietveld refinement of both the synchrotron diffraction powder (SPD) and the neutron diffraction powder (NPD) patterns was performed. The starting model was based on the $KCeF_4$ structure using the orthorhombic cell parameters previously determined. In a first step, SPD data were used to refine the cell parameters and the cationic positions. In a second step, the NPD pattern was used for refinement of the fluorine positions. The resulting model was finally refined using simultaneously the SPD and NPD data sets. For this last stage, individual histogram weighting was used to compensate the scale difference between both acquisitions (a 250 weighting factor was applied to the NPD data). This weighting did not induce any noticeable change on the SPD reliability factors. Small amounts of unreacted LaF_3 (0.9 wt %) and BN (0.7 wt %) originating from the sample holder during the synthesis step were also taken into account in the synchrotron data refinement. Considering the high statistics and high resolution of the data, very good reliability factors were obtained. Fourier difference maps (see Figure S2, Supporting Information) did not show any residue in the background. No splitting or abnormal anisotropy value has been detected either. The fits of the combined Rietveld refinement are shown in Figure 1. Atomic coordinates, thermal parameters, and La−F and Rb−F

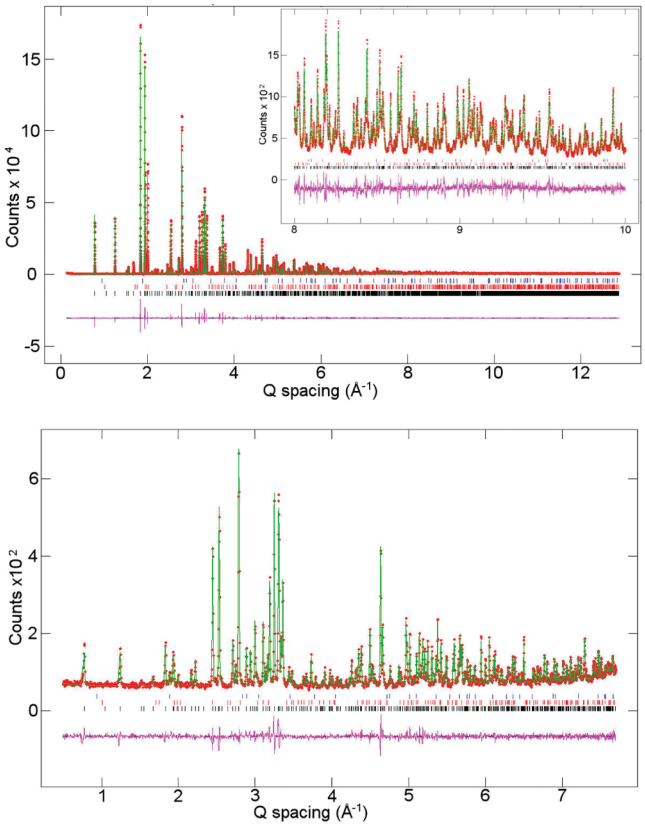

Figure 1. Rietveld refinements of the SPD (R_{wp} = 8.43%, R_p = 6.71%, and $R(F^2)$ = 2.81%, top) and NPD (R_{wp} = 5.30%, R_p = 4.08%, and $R(F^2)$ = 4.10%, bottom) patterns of $RbLaF_4$ recorded at room temperature. *Pnma* space group, a = 6.46281(2) Å, b = 3.86498(1) Å, and c = 16.17629(4) Å.

interatomic distances are gathered in Tables 1 and 2. The structure of $RbLaF_4$, which contains one La and one Rb

Table 1. Atomic Coordinates and Atomic Displacement Parameters (ADP in Å²) of $RbLaF_4$ (*Pnma*, a = 6.46281(2) Å, b = 3.86498(1) Å, c = 16.17629(4) Å) Determined from the Combined Rietveld Refinement of Both the SPD (APS-11BM) and the NPD (ILL-D2B) Patterns Collected at Room Temperature

atom	site	occ.	x	y	z	B_{eq} (Å²)
La	4c	1	0.25179(6)	1/4	0.44119(2)	0.56
Rb	4c	1	0.27509(8)	3/4	0.20070(3)	1.06
F1	4c	1	0.13392(11)	1/4	0.03695(5)	0.92
F2	4c	1	0.00067(10)	3/4	0.44397(5)	0.70
F3	4c	1	0.39137(12)	3/4	0.36973(5)	0.92
F4	4c	1	0.09340(12)	1/4	0.31114(5)	1.03

atom	U_{11} (*100)	U_{22} (*100)	U_{33} (*100)	U_{12} (*100)	U_{13} (*100)	U_{23} (*100)
La	0.68(2)	0.58(1)	0.86(2)	0	−0.04(2)	0
Rb	0.90(3)	1.79(3)	1.32(3)	0	0.07(2)	0
F1	0.82(4)	1.33(4)	1.36(4)	0	0.18(3)	0
F2	0.90(4)	0.83(4)	0.93(4)	0	0.40(3)	0
F3	1.49(4)	0.56(4)	1.45(4)	0	0.36(4)	0
F4	1.51(5)	1.46(4)	0.95(4)	0	−0.17(3)	0

crystallographic sites and four inequivalent F sites all located on 4c positions, is made up of alternating layers (perpendicular to the c direction) of LaF_9 edge-sharing polyhedra and RbF_7 edge-

Table 2. Rb−F and La−F Interatomic Distances (Å)

Rb−F2	2.757(1)	La−F1 (×2)	2.585(1)
Rb−F3	2.836(1)	La−F1	2.495(1)
Rb−F3	2.729(1)	La−F2 (×2)	2.524(1)
Rb−F4 (×2)	2.882(1)	La−F2	2.473(1)
Rb−F4 (×2)	2.829(1)	La−F3 (×2)	2.426(1)
		La−F4	2.340(1)

and face-sharing polyhedra (see Figure 2). The La and Rb coordination polyhedra can be described as a slightly distorted

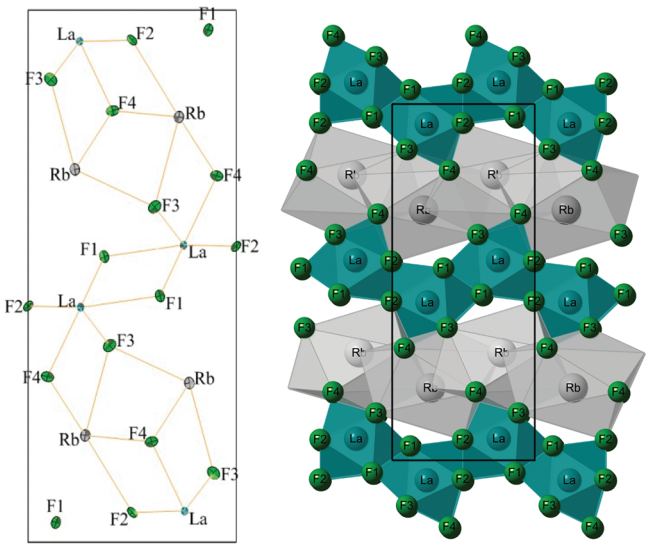

Figure 2. [010] view of the $RbLaF_4$ structure (right). Thermal ellipsoids are drawn at the 50% probability level (left).

tricapped trigonal prism and a monocapped trigonal prism, respectively (Figure S3, Supporting Information).

Solid-State NMR. High-resolution solid-state MAS NMR, allowing identification and quantification of the atomic local environments, was used to probe the number of inequivalent crystallographic sites in the $RbLaF_4$ structure.

The ^{87}Rb and ^{139}La MAS and static NMR spectra of $RbLaF_4$, recorded at high magnetic fields of 17.6 and 19.9 T with ^{19}F decoupling, are shown in Figures 3 and 4, respectively. For these two half-integer quadrupolar nuclei with relatively large quadrupolar moments (I = 3/2 with Q=133.5 mb for ^{87}Rb and I = 7.2 with Q = 200 mb for ^{139}La),[56] the observed MAS powder patterns are characteristic of single contributions with strong second-order quadrupolar broadening and give evidence for the presence of a single Rb and a single La crystallographic site in the structure, in agreement with the proposed model. Detailed inspection of the corresponding ^{87}Rb and ^{139}La high-field static spectra reveals extra features as compared to ideal quadrupolar lineshapes, testifying for the additional presence of significant chemical shift anisotropy (CSA) interactions. The interplay between the second-order quadrupolar and the CSA interactions strongly affects the singularity positions in static powder patterns, while it only modifies the spinning sideband intensities in fast-MAS spectra without changing the singularity positions. Since these two interactions exhibit different magnetic field dependences (i.e., second-order quadrupolar effects are scaled down when increasing the magnetic field while the CSA broadening increases linearly with the magnetic field),[57,58] simulation of spectra recorded at different magnetic

dx.doi.org/10.1021/ic202301e | Inorg. Chem. 2012, 51, 2272−2282

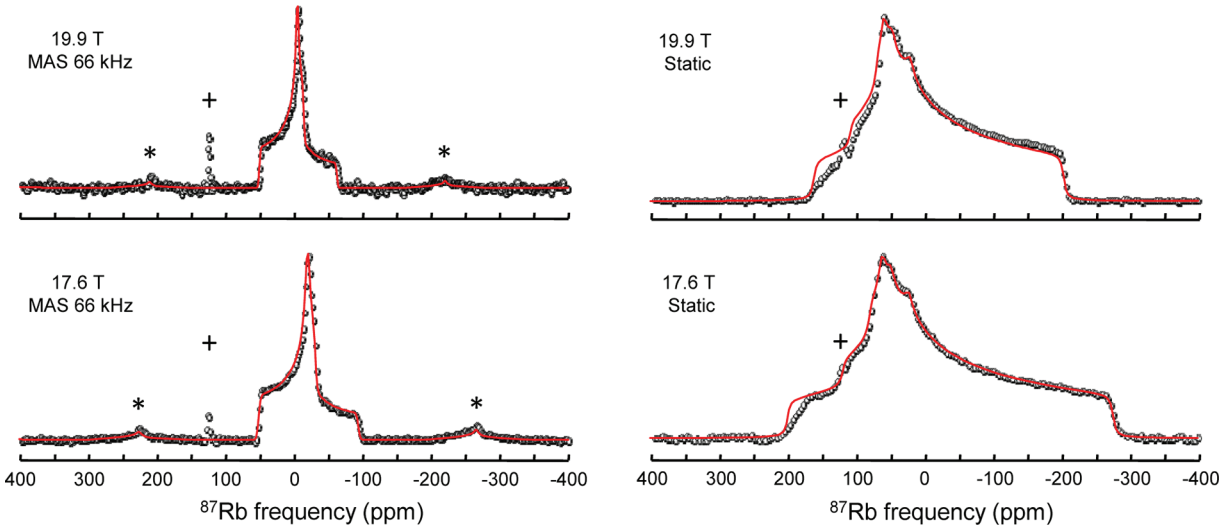

Figure 3. Experimental ^{87}Rb MAS and static NMR spectra of $RbLaF_4$ (dots) recorded with ^{19}F decoupling and their best fits (red lines): (top left) MAS 66 kHz at 19.9 T; (top right) static at 19.9 T; (bottom left) MAS 66 kHz at 17.6 T; (bottom right) static at 17.6 T. Cross indicates an unidentified impurity, and asterisks mark spinning sidebands.

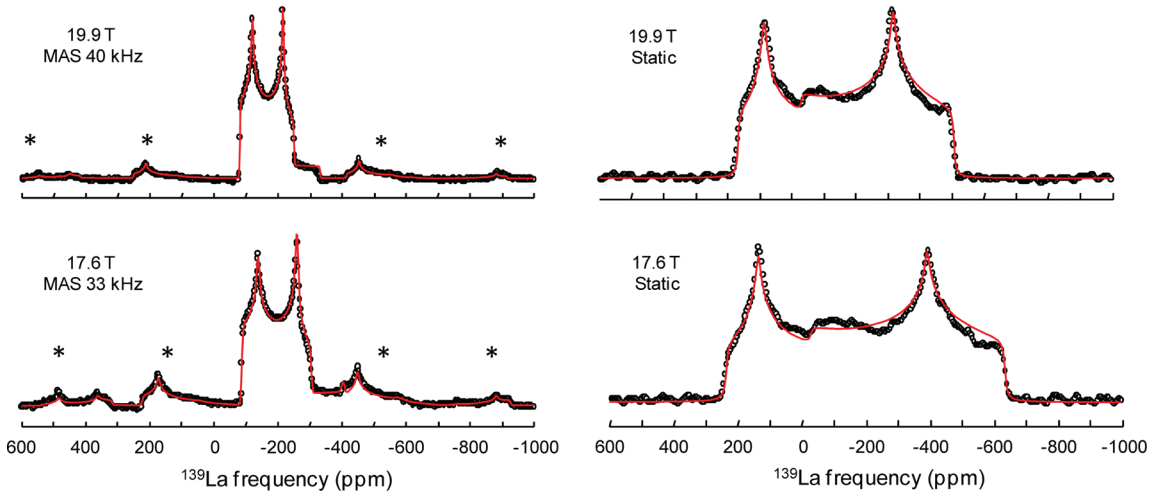

Figure 4. Experimental ^{139}La MAS and static NMR spectra of $RbLaF_4$ (dots) recorded with ^{19}F decoupling and their best fits (red lines): (top left) MAS 40 kHz at 19.9 T; (top right) static at 19.9 T; (bottom left) MAS 33 kHz at 17.6 T; (bottom right) static at 17.6 T. Asterisks mark spinning sidebands.

fields allows determining the quadrupolar coupling and CSA parameters as well as the three Euler angles (α, β, γ) specifying the relative orientation of the two tensors.[59−61] The isotropic chemical shifts, quadrupolar coupling, and CSA parameters and the relative orientation of the quadrupolar and CSA tensors determined by fitting simultaneously the static and MAS spectra recorded at 17.6 and 19.9 T are reported in Table 3. In $RbLaF_4$, the ^{87}Rb and ^{139}La nuclei exhibit relatively large quadrupolar coupling constants (C_Q = 10.97 and 24.65 MHz for ^{87}Rb and ^{139}La, respectively) and more moderate chemical shift anisotropies (δ_{CSA}= −28 and −27 ppm for ^{87}Rb and ^{139}La, respectively). For both ^{87}Rb and ^{139}La, the best fits of experimental spectra are obtained for α = 0° and β = 90° (i.e., the V_{zz} and δ_{xx} principal components of the quadrupolar and CSA tensors are aligned). However, since the ^{87}Rb and ^{139}La CSA asymmetry parameters are close to 1, nearly equivalent fits of the data sets can be obtained by exchanging δ_{xx} and δ_{zz} (i.e., changing the sign of δ_{CSA} with $\beta = 0° - V_{zz}$ and δ_{zz} aligned).

The ^{19}F *infinite spinning rate* MAS spectra of $RbLaF_4$ obtained from TOP processing[34] of the conventional MAS spectra recorded at 19.9 and 17.6 T (spinning frequency of 66 kHz) are presented in Figure 5. The spectrum obtained at 19.9 T exhibits four resolved resonances, two of them overlapping significantly at 17.6 T. The resonances located at 4.3 and −10.8 ppm clearly show non-Gaussian lineshapes (nearly pyramidal- and square-like lineshapes). To obtain further insight about the origin of these unusual lineshapes, additional ^{19}F MAS spectra were recorded at various spinning frequencies and at a lower magnetic field of 7.0 T (Figure S4, Supporting Information). All ^{19}F resonances exhibit a line broadening in Hertz independent of the field (corresponding to a narrowing in ppm) and a line width constant when increasing the spinning frequency from 50 to 66 kHz. These findings indicate that the observed lineshapes are not related to distributions of isotropic chemical shift nor dipolar couplings but originate from isotropic *J*-couplings. Evidence for the presence of significant heteronuclear ^{19}F−^{139}La *J*-couplings is provided by the 2D

Table 3. Experimental ^{87}Rb and ^{139}La Isotropic Chemical Shifts (δ_{ISO}), Chemical Shift Anisotropy (δ_{CSA}, η_{CSA}), Quadrupolar Coupling (C_Q, η_Q) Parameters, and Euler Angles (α, β, γ) Describing the Relative Orientation Between the CSA and Quadrupolar Tensors[a]

atom		δ_{ISO} (ppm)	C_Q (MHz)	η_Q	δ_{CSA} (ppm)	η_{CSA}	α (deg)	β (deg)	γ (deg)
^{87}Rb	exp.	51(1)	10.97(2)	1.0(1)	−28(2)	1.0(2)	0	90	50(5)
	calc. ES		10.99	0.94	−29	0.86	0	90	46
			10.98	*0.95*	*−30*	*0.72*	*0*	*90*	*45*
	calc. APO		11.06	0.90	−30	0.85	0	90	48
			11.40	*0.94*	*−30*	*0.80*	*0*	*90*	*44*
^{139}La	exp.	−59.5(5)	−24.65(2)	0.26(1)	−27(3)	0.8(1)	0	90	41(5)
	calc. ES		−24.50	0.30	−86	0.88	0	90	59
			−24.78	*0.32*	*−98*	*0.76*	*0*	*90*	*122*
	calc. APO		−21.11	0.20	−84	0.75	0	90	40
			−20.47	*0.34*	*−101*	*0.77*	*0*	*90*	*44*

[a]Calculated parameters ((δ_{CSA}, η_{CSA}, C_Q, η_Q, α, β, γ) using CASTEP[43,44] for the experimental (ES) and DFT atomic position optimized structure (APO) structures. Since only the absolute value of C_Q can be determined from NMR experiments on powdered samples, the sign of the experimental C_Q is set to the sign of the calculated C_Q. The chemical shift anisotropy (σ_{CSA}) values and asymmetry parameter (η_{CSA}) are defined as $\delta_{CSA} = (\delta_{zz} - \delta_{ISO})$ and $\eta_{CSA}=(\delta_{yy} - \delta_{xx})/\delta_{CSA}$, with the principal components of the CSA tensor defined as $|\delta_{zz} - \delta_{iso}| \geq |\delta_{xx} - \delta_{iso}| \geq |\delta_{yy} - \delta_{iso}|$. The calculated principal values of the CSA tensor were deduced from the calculated shielding tensor principal values using $\delta_{ii} = -(\sigma_{ii} - \sigma_{ref})$. The quadrupolar coupling constant (C_Q) and asymmetry parameter (η_Q) are defined as $C_Q = (eQV_{zz})/h$ and $\eta_Q = (V_{xx} - V_{yy})/V_{zz}$ with the principal components of the EFG tensor defined in the sequence $|V_{zz}| \geq |V_{yy}| \geq |V_{xx}|$. The quadrupolar moments (Q) of ^{87}Rb and ^{139}La were taken from ref 56. The values given in italics correspond to calculations performed without the 4f shift of 4.55 eV in the La USPP.

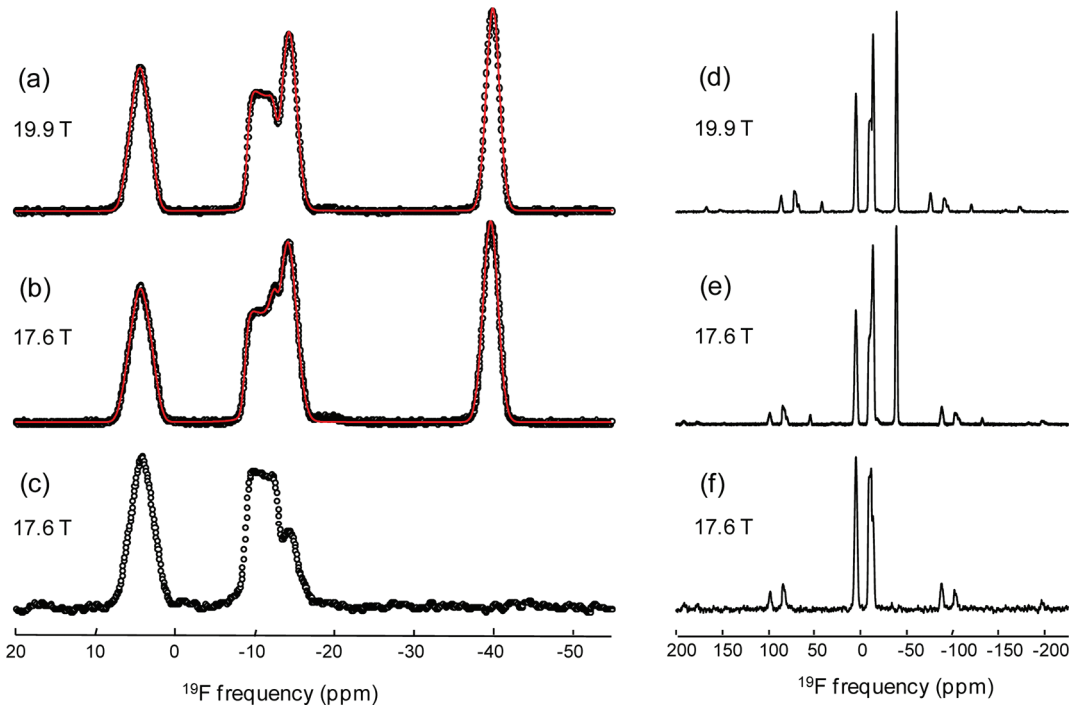

Figure 5. (a and b) Quantitative "infinite spinning frequency" ^{19}F MAS NMR spectra of $RbLaF_4$ (dots) and their best fits (red lines). (c) "Infinite spinning frequency" ^{19}F−{^{87}Rb} HMQC MAS spectrum. Spectra in a−c were obtained from the TOP processing[34] of the conventional MAS spectra recorded at 19.9 (d) and 17.6 T (e) with a spinning frequency of 66 kHz and of the 1D ^{19}F−{^{87}Rb} HMQC MAS spectrum recorded at 17.6 T with a spinning frequency of 66 kHz (f).

heteronuclear double-quantum (DQ) filtered *J*-resolved MAS experiment.[35] In this experiment, a DQ filter with ^{139}La CT-selective 90° pulses is used to select the *J*-multiplet components involving ^{139}La ± 1/2 Zeeman states for which a *J*-modulation is observed in an usual *J*-resolved experiment with ^{139}La CT-selective refocusing pulse, the lines associated only to ^{139}La outer Zeeman states (unaffected by the CT-selective refocusing pulse) being filtered out. For a ^{19}F nucleus coupled to n ^{139}La atoms (99.9% natural abundance and nuclear spin $I = 7/2$) with the same *J*-coupling constants the components associated to k ($1 \leq k \leq n$) ^{139}La nuclei in ±1/2 Zeeman states are thus selected, leading to a line narrowing in the DQ-filtered dimension and to observation of n overlapping simplified multiplets of $k + 1$ lines (with relative intensities depending on the DQ filtering time) in the projection of the 2D spectrum along the *J*-resolved dimension. This is clearly illustrated in Figure 6a, which displays the obtained 2D spectrum. Importantly, it should be noticed that the lines of the multiplet associated to the ±1/2 Zeeman states of an half-integer quadrupolar nucleus are equally shifted by the residual dipolar

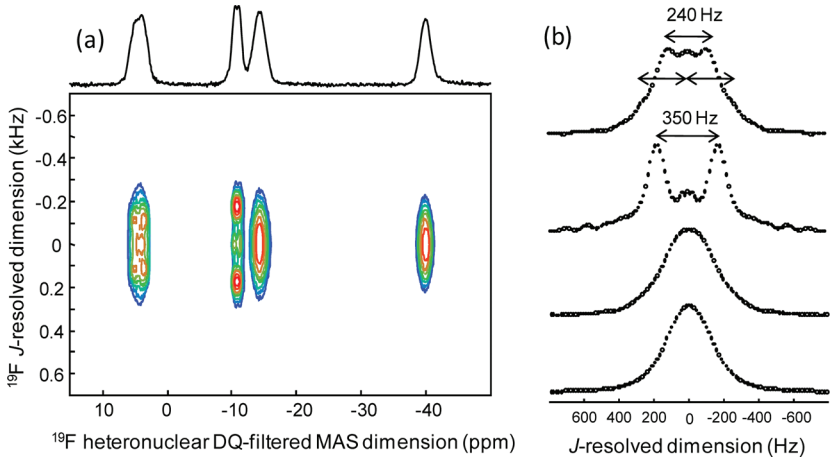

Figure 6. (a) 2D heteronuclear DQ-filtered $^{19}F-^{139}La$ *J*-resolved MAS spectrum of $RbLaF_4$ recorded at 19.9 T with a spinning frequency of 65 kHz. (b) Projections in the *J*-resolved dimension of the ^{19}F resonances located at 4.3, −10.8, −14.3, and −39.8 ppm (from top to bottom).

splitting due to second-order quadrupole−dipole cross terms.[62,63] Therefore, the splittings observed in the *J*-resolved dimension of the 2D spectrum are unaffected by second-order effects, allowing direct measurement of the *J*-coupling constants. For the ^{19}F resonances located at −10.8 and 4.3 ppm, a significant line narrowing is observed in the DQ-filtered MAS dimension and isotropic $^1J(^{19}F-^{139}La)$ couplings are clearly resolved as a doublet (^1J = 350 Hz) and overlapping doublet and triplet (^1J = 240 Hz) in the indirect *J*-resolved dimension (Figure 6b). According to these patterns, the two resonances at −10.8 and 4.3 ppm are unambiguously assigned to the F4 and F3 sites of the structure, which are, respectively, bonded to one and two La atoms (see Table 2). For the two remaining resonances at located −14.3 and −39.8 ppm, associated to F_1 and F_2 which are both bonded to three La atoms, the *J*-multiplet patterns are not resolved, revealing significantly weaker *J*-coupling constants. Assuming that all ^{19}F resonances have almost similar nonrefocusable linewidths (i.e., in the 130−150 Hz range), these *J*-coupling constant can be estimated to be smaller than 170 Hz. Very good fits of the ^{19}F quantitative MAS spectra (Figure 5) are obtained using two broadened *J*-multiplet patterns with $^1J(^{19}F-^{139}La)$ coupling constants of 240 and 350 Hz for the F3 and F4 resonances and two Gaussian lines for the resonances at −14.3 and −39.8 ppm with relative intensities in a 1:1:1:1 ratio, in agreement with the crystallographic site multiplicities. In this case, residual dipolar splittings (RDS) have to be considered to account for the slight asymmetry of the pyramidal- and square-like shapes of the F3 and F4 resonances in MAS spectra (see Figure S5, Supporting Information). Due to the lack of resolution of the individual components of the *J* multiplet pattern, the *J*-coupling anisotropy and the Euler angles specifying the orientation of the $^{19}F-^{139}La$ dipolar vectors in the ^{139}La quadrupolar tensor frame cannot be unambiguously determined from simulation of MAS spectra. Therefore, only the magnitude of the RDS term was fitted using a simplified model.[63] Since a final assignment of the resonances at −14.3 and −39.8 ppm cannot be made on the basis of $^1J(^{19}F-^{139}La)$ coupling constants, a 1D $^{19}F-^{87}Rb$ HMQC MAS experiment[36−38] allowing selective observation of the fluorine ions bonded to Rb atoms was additionally performed. As shown in Figure 5c, the resonance at −39.8 ppm is filtered out the obtained spectrum and is thus unambiguously assigned to F1, which is the only fluorine site without any F−Rb bonds (see Table 2). Consequently, the resonance at −14.3 ppm is assigned to the remaining F2 site. It should be mentioned that the isotropic $^1J(^{19}F-^{87}Rb)$ couplings and/or residual dipolar splittings, which drive the coherence transfer in the HMQC MAS experiments,[64,65] were not resolved in $^{19}F-^{87}Rb$ DQ-filtered *J*-resolved spectra and are smaller than the ^{19}F nonrefocusable linewidths.

The ^{19}F resonances assignment described above are furthermore supported by ^{19}F homonuclear through-space correlation MAS NMR experiments based on $^{19}F-^{19}F$ dipolar couplings (directly related to the F−F distances), which have been successfully used to probe F−F short-range proximities (up to ∼4.5 Å) in fluorides.[66−69] In the ^{19}F double-quantum single-quantum through-space MAS correlation spectrum of $RbLaF_4$ (Figure 7) recorded using the DH^3 experiment,[39]

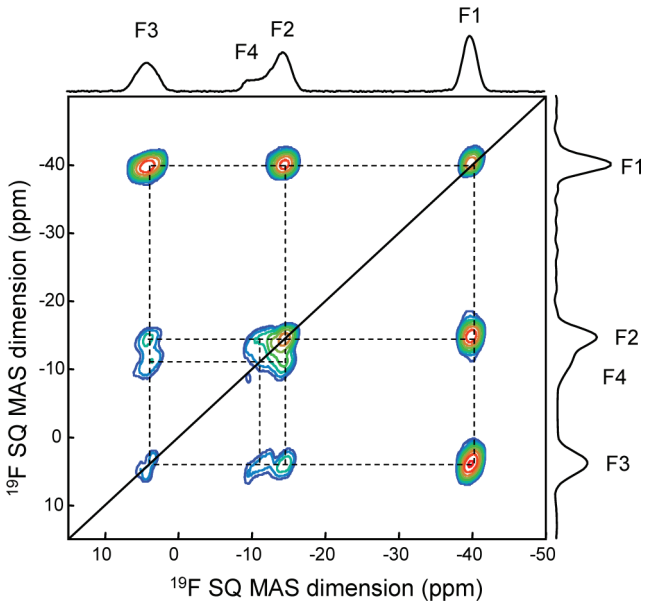

Figure 7. 2D ^{19}F homonuclear DS-SQ correlation MAS spectrum recorded at 17.6 T using the DH^3 experiment with a spinning frequency of 66 kHz. Spectrum is represented in a SQ−SQ format after a shearing transformation of the data set. Solid line indicates the diagonal of the spectrum on which autocorrelation peaks appear, and dashed lines show paired cross-correlation peaks.

dx.doi.org/10.1021/ic202301e | Inorg. Chem. 2012, 51, 2272−2282

proximities between different fluorine sites, and proximities between equivalent F sites are evidenced by cross- and autocorrelation peaks, respectively, with relative intensities proportional to the square of the sum of r^{-3} (r being the interatomic distance).[69,39] According to F−F distances and correlation peak relative intensities (Tables S1 and S2, Supporting Information), the resonance at −39.8 ppm, which shows an intense autocorrelation and two intense cross-correlation peaks, is unambiguously assigned to F1, while the resonance at −14.3 ppm exhibiting one auto- and one cross-correlation (with F1) peak of high intensity is assigned to F2. The resonance at 4.3 ppm, which shows only a strong cross-correlation peak with F1, is assigned to F3. The remaining peak at −10.8 ppm thus corresponds to F4.

DFT Calculations of NMR Parameters. Recently, first-principles computation of the NMR chemical shifts has been introduced as an efficient method for structure refinement of organic solids[70−73] and zeolites.[74,75] First-principles calculations of the NMR quadrupolar parameters were also used for structural model validation in the case of inorganic fluorides.[76,77] Therefore, we carried out DFT computations of NMR parameters as final criterion to validate the $RbLaF_4$ proposed structural model. For this purpose, we used the PAW[45] and GIPAW[46] methods implemented in the CASTEP code,[43,44] which use periodic boundary conditions and enable efficient and accurate calculation of the chemical shielding and electric field gradient (EFG) tensors for a wide range of crystalline systems.[45,78−85] Computations were performed for both the refined and the PBE-DFT atomic position-optimized (APO) structures.

For both ^{87}Rb and ^{139}La, the NMR interaction parameters calculated from the refined structure are in good agreement with the experimentally measured values (see Table 3), except only for the calculated ^{139}La CSA value, which is somewhat overestimated. For the APO structure, a slightly less good agreement between experimental and calculated values is observed, in particular for the ^{139}La and ^{87}Rb quadrupolar coupling parameters. It should be noted that all atomic positions are expected to be very accurately determined from the combined refinement of powder neutron and synchrotron diffraction data. In such a case, the small variation of the structural parameters induced by PBE-DFT geometry optimization may lead to less accurate calculated NMR parameters, the PBE functional being known to slightly overestimate the bond lengths.[86,87] The ^{19}F isotropic chemical shifts determined from the GIPAW calculated ^{19}F isotropic shielding constants using the relationship given in ref 49 are reported in Table 4. The ^{19}F experimental chemical shift anisotropy (CSA) parameters determined from the spinning sidebands intensities in MAS spectra recorded at spinning frequencies of 28 and 40 kHz (neglecting ^{19}F−^{139}La J couplings and residual dipolar splitting) are also given in Table 4 together with the GIPAW-calculated values. A very nice agreement between experimental and predicted ^{19}F isotropic chemical shift values is obtained whatever the structures (refined or APO) used for the calculations. Similarly, the calculated CSA parameters for the F1 and F2 resonances are very close to the experimental values. In the case of the F3 and F4 resonances (corresponding to the F sites with the shortest La−F bond lengths), the agreement between experimental and calculated CSA values is slightly less good. On the basis of these calculations, the refined and APO structures cannot be distinguished. It should be noted that, as discussed in ref 49 and illustrated in Table 4, a shift to higher energy (4.55 eV) of the La 4f orbitals in the La USPP is required to calculate more accurately the ^{19}F isotropic shielding tensors. However, the results obtained here suggest that the value of the applied 4f shift should be further refined to improve the agreement between the experimental and the calculated CSA values for both ^{139}La and the F3 and F4 resonances.

Table 4. Experimental and DFT-GIPAW Calculated for the Experimental (ES) and Atomic Position Optimized (APO) Structures ^{19}F Isotropic Chemical Shifts (δ_{ISO}) and Chemical Shift Anisotropy Parameters (δ_{CSA}, η_{CSA}) in $RbLaF_4$[a]

site		σ_{ISO} (ppm)	δ_{ISO} (ppm)	δ_{CSA} (ppm)	η_{CSA}
F1	exp.		−39.8(2)	−59(2)	0.46(5)
	calc. ES	160.1	−39.1	−56	0.39
		122.8	*−9.2*	*-66*	*0.47*
	calc. APO	157.7	−37.2	−56	0.47
		123.0	*−9.4*	*−68*	*0.46*
F2	exp.		−14.3(2)	−51(2)	0.34(5)
	calc. ES	133.1	−17.5	−47	0.22
		96.4	*11.9*	*−57*	*0.41*
	calc. APO	132.1	−16.6	−47	0.32
		96.7	*11.6*	*−57*	*0.43*
F3	exp.		4.3(3)	110(4)	0.32(5)
	calc. ES	108.4	2.3	130	0.27
		71.4	*31.9*	*151*	*0.34*
	calc. APO	105.5	4.6	130	0.22
		70.6	*32.5*	*152*	*0.33*
F4	exp.		−10.8(2)	−120(4)	0.33(5)
	calc. ES	128.8	−14.0	−156	0.32
		99.5	*9.4*	*−187*	*0.28*
	calc. APO	127.9	−13.3	−151	0.30
		95.7	*12.4*	*−191*	*0.27*

[a]The calculated isotropic chemical shifts were deduced from the calculated isotropic chemical shielding (σ_{ISO}) values using the relationship $\delta_{ISO} = -0.8\ \sigma_{ISO} + 89$.[49] The chemical shift anisotropy and asymmetry parameters are defined as $\delta_{CSA} = (\delta_{zz} - \delta_{ISO}) = (\sigma_{ISO} - \sigma_{zz})$ and $\eta_{CSA} = |(\delta_{YY} - \delta_{XX})/(\delta_{CSA})| = |(\sigma_{XX} - \sigma_{YY})/(\sigma_{CSA})|$, with the principal components of the chemical shift and chemical shielding tensors defined as $|\delta_{zz} - \delta_{ISO}| \geq |\delta_{xx} - \delta_{ISO}| \geq |\delta_{yy} - \delta_{ISO}|$ and $|\sigma_{ISO} - \sigma_{zz}| \geq |\sigma_{ISO} - \sigma_{xx}| \geq |\sigma_{ISO} - \sigma_{yy}|$, respectively. The values given in italics correspond to calculations performed without the 4f shift of 4.55 eV in the La USPP.

Electrical Conductivity of $RbLaF_4$ and Luminescence of Eu-Doped $RbLaF_4$. Numerous rare-earth fluoride compounds are known to exhibit high ionic conductivity.[1] Rare-earth-doped fluorides also show interesting luminescence properties.[5−8] Therefore, the conductivity as a function of temperature in $RbLaF_4$ and the luminescence properties of Eu-doped $RbLaF_4$ have been additionally investigated.

The electrical conductivity of $RbLaF_4$ was determined by impedance spectroscopy in the 147−387 °C temperature range under dry nitrogen atmosphere. Below 147 °C, impedance diagrams do not reveal electrical conductivity. Figure 8a shows a typical impedance spectrum (Nyquist plot) obtained for $RbLaF_4$ at 387 °C. At high frequency, this spectrum exhibits two different overlapping semicircles, which can be satisfactorily least-squares adjusted with a series combination of two R//CPE elements of the Z-view 3.3a software[50] (where R is a pure resistance and CPE is a constant phase element, representing the conductive and dipolar part of the sample, respectively). The former arc is assigned to the bulk response, and the latter one is associated to the grain boundaries contribution. The low-

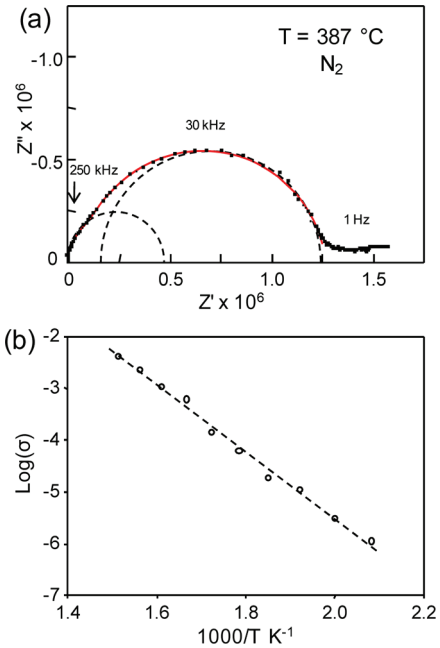

Figure 8. (a) Representative Nyquist plot of complex impedance spectrum collected at 387 °C on $RbLaF_4$ pellets in a N_2 atmosphere. (b) Temperature dependence of the electrical conductivity of $RbLaF_4$ fitted with a conventional Arrhenius law.

frequency part of the impedance plot, which could not only be ascribed to usual polarization electrode phenomenon, was not taken into account in the adjustment. In the temperature range from 207 to 387 °C, the two relaxation phenomena associated to the bulk and the grain boundary conductivities were separately refined, while below 207 °C only a total resistance was measured since both contributions cannot be clearly distinguished. As shown in Figure 8b, evolution of the bulk conductivity as a function of temperature is nicely modeled with a conventional Arrhenius low ($\log(\sigma T) = \log(\sigma_0) - E_A/kT$) with an activation energy E_A = 1.28 eV. At 387 °C, the bulk conductivity is $\sigma = 6.1 \times 10^{-6}$ S·cm^{-1} and at 127 °C the total conductivity is $\sigma = 3.1 \times 10^{-11}$ S·cm^{-1}. As expected from the determined structure having crystallographic sites fully occupied, this undoped material exhibits low conductivity values. These are several orders of magnitude lower than those reported for well-known fluoride ionic conductors with tysonite structure[88] (LaF_3) or fluorite-type structure[89,90] (β-$PbSnF_4$, $RbBiF_4$).

The excitation spectrum (monitored at 613 nm) recorded for the 5% Eu-doped $RbLaF_4$ sample is shown in Figure 9a. This spectrum consists of several bands in the 200−500 nm range relatively similar to those reported for the hexagonal $NaYF_4$,[91] which can be attributed to excitation of the Eu^{3+} cations from the ground state to higher levels of the 4f manifold. The emission spectrum of this sample (Figure 9b) was obtained using an excitation wavelength of 393 nm, which corresponds to the most intense excitation band ($^7F_0$−$^5L_6$ transition). This spectrum displayed the emissions characteristic of the Eu^{3+} cations, most of them (λ > 570 nm) due to the $^5D_0$−^7F_J (J = 1, 2, 3, and 4) electronic transitions (Figure 9b). The most intense emissions appeared in the 580−620 nm range, which are responsible for the strong orange-red luminescence observed for this sample (Figure 9b, inset). It is important to mention that the relative intensity of the $^5D_0$−$^7F_2$ emission

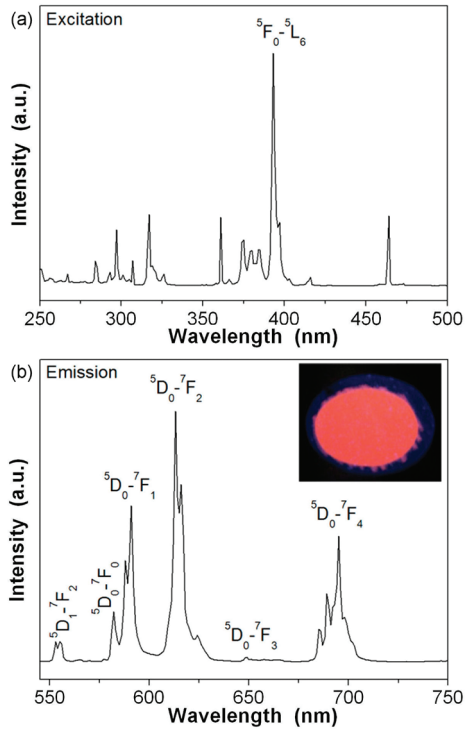

Figure 9. (a) Excitation (λ_{em} = 613 nm) and (b) emission (λ_{ex} = 393 nm) spectra of the 5% Eu^{3+}-doped $RbLaF_4$ sample. (Inset) Picture of the Eu:$RbLaF_4$ sample recorded under UV illumination.

band was higher than that associated to the $^5D_0$−$^7F_1$ transition, which is expected for Eu^{3+} cations located in crystallographic sites without an inversion center, as it is the case of the irregular La−F polyhedron of the $RbLaF_4$ orthorhombic structure, thus confirming incorporation of the Eu^{3+} cations within the $RbLaF_4$ structure.

■ CONCLUSION

The crystal structure $RbLaF_4$ has been resolved by combining neutron and synchrotron powder diffraction data refinements. The $RbLaF_4$ orthorhombic structure (*Pnma*, a = 6.46281(2) Å, b = 3.86498(1) Å, c = 16.17629(4) Å, Z = 4) contains one Rb and one La crystallographic sites and four inequivalent F sites located on 4c positions. It is made up of an alternation of LaF_9 and RbF_7 polyhedra layers. $RbLaF_4$ exhibits a low ionic conductivity from room temperature up to 400 °C. A strong red-orange luminescence in Eu-doped sample is observed under excitation at 393 nm. ^{87}Rb, ^{139}La, and ^{19}F solid-state MAS NMR spectra, which allow evidencing the number of inequivalent crystallographic sites, are in agreement with the proposed structural model. Assignment of the ^{19}F resonances is performed on the basis of both ^{19}F−^{139}La J-coupling multiplet patterns observed in a heteronuclear DQ-filtered J-resolved spectrum and ^{19}F−^{87}Rb HMQC MAS experiments. To further confirm the accuracy of the proposed structure, DFT calculations of both ^{19}F isotropic chemical shieldings and ^{87}Rb, ^{139}La electric field gradient tensors were performed using the GIPAW and PAW methods implemented in the CASTEP code. It is found that the calculated values are in good agreement with the experimental ones.

■ ASSOCIATED CONTENT

Supporting Information

$RbLaF_4$ CIF file, X-ray diffraction powder patterns of $RbLaF_4$ recorded at different temperatures, Fourier observed and difference maps of the neutron refinement, pictures of the Rb and La coordination polyhedra, ^{19}F MAS NMR spectra of $RbLaF_4$ recorded at high and low magnetic fields, F−F interatomic distances (Å) with a cutoff of 4.5 Å, normalized F−F correlation peak relative intensities (±0.04) in the experimental ^{19}F DQ-SQ MAS correlation spectrum; expansion of the experimental ^{19}F MAS spectrum of $LaRbF_4$ recorded at 19.9 T with a spinning frequency of 66 kHz and best fits taken into account or disregarding residual dipolar splitting; exact simulations of the F4 resonance line shape with and without residual dipolar splitting for various Gaussian broadenings; experimental ^{19}F MAS spectra recorded at 17.6 T with spinning frequencies of 26 and 40 kHz used to determine the ^{19}F chemical shift anisotropy parameters from spinning sideband intensities. This material is available free of charge via the Internet at http://pubs.acs.org.

■ AUTHOR INFORMATION

Corresponding Author

*E-mail: anne-laure.rollet@upmc.fr.

■ ACKNOWLEDGMENTS

The authors thank Eric Labrude for the boron nitride crucibles machining and Sandra Ory for DSC measurements. Use of the Advanced Photon Source at Argonne National Laboratory was supported by the U.S. Department of Energy, Office of Science, Office of Basic Energy Sciences, under Contract No. DE-AC02-06CH11357. Financial support from the TGIR RMN THC FR3050 is gratefully acknowledged. The computations presented in this work have been carried out at the "Centre de Calcul Scientifique en Région Centre" facility (CCRS, Orléans, France) under the CASCIMODOT program.

■ REFERENCES

(1) Sorokin, N. I.; Sobolev, B. P. *Crystallogr. Rep.* **2007**, *52*, 842−863.
(2) Godard, A. *C. R. Phys.* **2007**, *8*, 1100−1128.
(3) Phillips, J. M.; Coltrin, M. E.; Crawford, M. H.; Fischer, A. J.; Krames, M. R.; Mueller-Mach, R.; Mueller, G. O.; Ohno, Y.; Rohwer, L. E. S.; Simmons, J. A.; Tsao, J. Y. *Laser Photonics Rev.* **2007**, *1*, 307−333.
(4) Setlur, A. A.; Radkov, E. V.; Henderson, C. S.; Her, J.-H.; Srivastava, A. M.; Karkada, N. M.; Kishore, S.; Kumar, N. P.; Aesram, D.; Deshpande, A.; Kolodin, B.; Grigorov, L. S.; Happek, U. *Chem. Mater.* **2010**, *22*, 4076−4082.
(5) Pierrard, A.; Gredin, P.; de Kozak, A.; Viana, B.; Aschehoug, P.; Vivien, D.; Derouet, J.; Bourée-Vigneron, F. *Phys. Status Solidi* **2001**, *226*, 329−338.
(6) Zakaria, D.; Mahiou, R.; Avignant, D.; Zahir, M. *J. Alloys Compd.* **1997**, *257*, 65−68.
(7) Dominiak-Dzik, G.; Gołab, S.; Bałuka, M.; Pietraszko, A.; Hermanowicz, K. *J. Phys.: Condens. Matter* **1999**, *11*, 5245−5256.
(8) You, F.; Huang, S.; Liu, S.; Tao, Y. *J. Solid State Chem.* **2004**, *177*, 2777−2782.
(9) Goto, T.; Nohira, T.; Hagiwara, R.; Ito, Y. *J. Fluorine Chem.* **2009**, *130*, 102−107.
(10) Lacquement, J.; Boussier, H.; Laplace, A.; Conocar, O.; Grandjean, A. *J. Fluorine Chem.* **2009**, *130*, 18−21.
(11) Nuttin, A.; Heuer, D.; Billebaud, A.; Brissot, R.; Le Brun, C.; Liatard, E.; Loiseaux, J.-M.; Mathieu, L.; Meplan, O.; Merle-Lucotte, E.; Nifenecker, H.; Perdu, F.; David, S. *Prog. Nucl. Energy* **2005**, *46*, 77−99.
(12) Mathieu, L.; Heuer, D.; Brissot, R.; Garzenne, C.; Le Brun, C.; Lecarpentier, D.; Liatard, E.; Loiseaux, J.-M.; Meplan, O.; Merle-Lucotte, E.; Nuttin, A.; Walle, E.; Wilson, J. *Prog. Nucl. Energy* **2006**, *48*, 664−679.
(13) Rollet, A.-L.; Bessada, C.; Rakhmatoulline, A.; Auger, Y.; Melin, P.; Gailhanou, M.; Thiaudiere, D. *C. R. Chim.* **2004**, *7* (12), 1135−1140.
(14) Bessada, C.; Rollet, A.-L.; Rakhmatullin, A.; Nuta, I.; Florian, P.; Massiot, D. *C. R. Chim.* **2006**, *9*, 374−380.
(15) Pauvert, O; Zanghi, D.; Salanne, M.; Simon, C.; Rakhmatullin, A.; Matsuura, H.; Okamoto, Y.; Vivet, F.; Bessada, C. *J. Phys. Chem. B* **2010**, *114*, 6472−6479.
(16) Watanabe, S.; Adya, A. K.; Okamoto, Y.; Umesaki, N.; Honma, T.; Deguchi, H.; Horiuchi, M.; Yamamoto, T.; Noguchi, S.; Takase, K.; Kajinami, A.; Sakamoto, T.; Hatcho, M.; Kitamura, N.; Akatsuka, H.; Matsuura, H. *J. Alloys Compd.* **2006**, *408−412*, 71−75.
(17) Matsuura, H.; Watanabe, S.; Akatsuka, H.; Okamoto, Y.; Adya, A. K. *J. Fluorine Chem.* **2009**, *130*, 53−60.
(18) Bessada, C.; Rakhmatullin, A.; Rollet, A.-L.; Zanghi, D. *J. Fluorine Chem.* **2009**, *130*, 45−52.
(19) Rollet, A.-L.; Godier, S.; Bessada, C. *Phys. Chem. Chem. Phys.* **2008**, *10*, 3222−3228.
(20) Fedorov, P. P. *Russ. J. Inorg. Chem.* **1999**, *44*, 1703−1727.
(21) Beneš, O.; Konings, R. J. M. *CALPHAD* **2008**, *32*, 121−128.
(22) Abdoun, F.; Gaune-Escard, M.; Hatem, G. *J. Phase Equilib.* **1997**, *18*, 6−20.
(23) Lage, M. M.; Matinaga, F. M.; Gesland, J.-Y.; Moreira, R. L. *J. Appl. Phys.* **2006**, *99*, 053510.
(24) Zachariasen, W. H. *Acta Crystallogr.* **1949**, *2*, 388−390.
(25) Schmutz, H. Thesis, Institut für Radiochemie, Karlsruhe, Germany, 1966.
(26) Sarakovskis, A.; Grube, J.; Mishnev, A.; Spingis, M. *Opt. Mater.* **2009**, *31*, 1517−1524.
(27) Tyagi, N.; Reddy, A. A.; Nagarajan, R. *Opt. Mater.* **2010**, *33*, 42−47.
(28) Filatova, T. G.; Zakharova, B. S.; Reshetnikova, L. P.; Novoselova, A. V. *Zh. Neorg. Khim.* **1980**, *25* (5), 1427−1429; *Russ. J. Inorg. Chem. (Engl. Transl.)* **1980**, *25* (5), 793−794.
(29) Powder Diffraction File; Kabekkodu, S., Ed.; International Centre for Diffraction Data: Newtown Square, PA, 2007.
(30) Larson, A. C.; Von Dreele, R. B. *General Structure Analysis System (GSAS)*, Report LAUR 86-748; Los Alamos National Laboratory: Los Alamos, NM, 2000.
(31) Toby, B. H. *J. Appl. Crystallogr.* **2001**, *34*, 210−213.
(32) Detken, A.; Hardy, E. H.; Ernst, M.; Meier, B. H. *Chem. Phys. Lett.* **2002**, *356*, 298−304.
(33) Blümich, B.; Blumler, P.; Jansen, J. *Solid State NMR* **1992**, *1*, 111−113.
(34) Massiot, D.; Hiet, J.; Pellerin, N.; Fayon, F.; Deschamps, M.; Steuernagel, S.; Grandinetti, P. J. *J. Magn. Reson.* **2006**, *181*, 310−315.
(35) Martineau, C; Fayon, F.; Legein, C.; Buzaré, J.-Y.; Silly, G.; Massiot, D. *Chem. Commun.* **2007**, 2720−2722.
(36) Franke, D.; Banks, K.; Eckert, H. *J. Phys. Chem.* **1992**, *96*, 11048−11054.
(37) Lesage, A.; Sakellariou, D.; Steuernagel, S.; Emsley, L. *J. Am. Chem. Soc.* **1998**, *120*, 13194−13201.
(38) Massiot, D.; Fayon, F.; Alonso, B.; Trebosc, J.; Amoureux, J.-P. *J. Magn. Reson.* **2003**, *164*, 160−164.
(39) Deschamps, M.; Fayon, F.; Cadars, S.; Rollet, A.-L.; Massiot, D. *Phys. Chem. Chem. Phys.* **2011**, *13*, 8024−8030.
(40) Harris, R. K.; Becker, E. D.; Cabral de Menezes, S. M.; Goodfellow, R.; Granger, P. *Pure Appl. Chem.* **2001**, *73*, 1795−1818.
(41) Massiot, D.; Fayon, F.; Capron, M.; King, I. J.; Le Calvé, S.; Alonso, B.; Durand, J. O.; Bujoli, B.; Gan, Z.; Hoatson, G. *Magn. Reson. Chem.* **2002**, *40*, 70−76.
(42) Eichele, W. *WSolids1 NMR Simulation Package*, ver. 1.20.15, Tübingen Universität: Germany, 2011.

(43) Segall, M. D.; Lindan, P. L. D.; Probert, M. J.; Pickard, C. J.; Hasnip, P. J.; Clark, S. J.; Payne, M. C. *J. Phys.: Condens. Matter* **2002**, *14*, 2717−2744.
(44) Clark, S. J.; Segall, M. D.; Pickard, C. J.; Hasnip, P. J.; Probert, M. J.; Refson, K.; Payne, M. C. *Z. Kristallogr.* **2005**, *220*, 567−570.
(45) Profeta, M.; Mauri, F; Pickard, C. J. *J. Am. Chem. Soc.* **2003**, *125*, 541−548.
(46) Pickard, C. J.; Mauri, F. *Phys. Rev. B* **2001**, *63*, 245101.
(47) Perdew, J. P.; Burke, K.; Ernzerhof, M. *Phys. Rev. Lett.* **1996**, *77*, 3865−3868.
(48) Yates, J. R.; Pickard, C. J.; Mauri, F. *Phys. Rev. B* **2007**, *76*, 024401.
(49) Sadoc, A.; Body, M.; Legein, C.; Biswal, M.; Fayon, F.; Rocquefelte, X.; Boucher, F. *Phys. Chem. Chem. Phys.* **2011**, *13*, 18539−18550.
(50) *Z-view*, version 3.3a; Scribner Associates Inc.: Southern Pines, NC.
(51) Boultif, A.; Louër, D. *J. Appl. Crystallogr.* **1991**, *24*, 987−993.
(52) Werner, P.-E. *Z. Kristallogr.* **1964**, *120*, 375−387.
(53) Brunton, G. *Acta Crystallogr.* **1969**, *B25*, 600−602.
(54) Saf'yanov, Y. N.; Bochkova, R. I.; Kuz'min, E. A.; Belov, N. V. *Dokl. Akad. Nauk SSSR* **1973**, *212*, 96.
(55) Werner, F.; Weil, M.; Kubel, F. *Acta Crystallogr.* **2003**, *E59*, i47−i49 (Structure reports online).
(56) Pyykkö, P. *Mol. Phys.* **2008**, *106*, 1965−1974.
(57) Eckert, H. *Prog. Nucl. Magn. Reson. Spectrosc.* **1992**, *24*, 159−293.
(58) MacKenzie, K. J. D.; Smith, M. E. *Multinuclear Solid-State NMR of Inorganic Materials*; Pergamon: Amsterdam, 2002.
(59) Chu, P. J.; Gerstein, B. C. *J. Chem. Phys.* **1989**, *91*, 2081−2101.
(60) Cheng, J. T.; Edwards, J. C.; Ellis, P. D. *J. Phys. Chem.* **1990**, *94*, 553−561.
(61) Power, W. P.; Wasylishen, R. E.; Mooibroek, S.; Pettitt, B. A.; Danchura, W. *J. Phys. Chem.* **1990**, *94*, 591−598.
(62) Menger, M. E.; Veeman, W. S. *J. Magn. Reson.* **1982**, *46*, 257−268.
(63) Harris, R. K.; Olivieri, A. C. *Prog. Nucl. Magn. Reson. Spectrosc.* **1992**, *24*, 435−456.
(64) Cavadini, S.; Lupulescu, A.; Antonijevic, S.; Bodenhausen, G. *J. Am. Chem. Soc.* **2006**, *128*, 7706−7707.
(65) Cavadini, S.; Antonijevic, S.; Lupulescu, A.; Bodenhausen, G. *J. Magn. Reson.* **2006**, *182*, 168−172.
(66) Alam, T. M.; Clawson, J. S.; Bonhomme, F.; Thoma, S. G.; Rodriguez, M. A.; Zheng, S.; Autschbach, J. *Chem. Mater.* **2008**, *20*, 2205−2217.
(67) Martineau, C.; Fayon, F.; Legein, C.; Buzaré, J.-Y.; Goutenoire, F.; Suard, E. *Inorg. Chem.* **2008**, *47*, 10895−10905.
(68) Martineau, C.; Legein, C.; Buzaré, J.-Y.; Fayon, F. *Phys. Chem. Chem. Phys.* **2009**, *11*, 950−957.
(69) Wang, Q.; Hu, B.; Fayon, F.; Trebosc, J.; Legein, C.; Lafon, O.; Deng, F.; Amoureux, J.-P. *Phys. Chem. Chem. Phys.* **2009**, *11*, 10391−10395.
(70) Pickard, C. J.; Salager, E.; Pintacuda, G.; Elena, B.; Emsley, L. *J. Am. Chem. Soc.* **2007**, *129*, 8932−8933.
(71) Salager, E.; Stein, R. S.; Pickard, C. J.; Elena, B.; Emsley, L. *Phys. Chem. Chem. Phys.* **2009**, *11*, 2610−2621.
(72) Salager, E.; Day, G. M.; Stein, R. S.; Pickard, C. J.; Elena, B.; Emsley, L. *J. Am. Chem. Soc.* **2010**, *132*, 2564−2566.
(73) Webber, A. L.; Emsley, L.; Claramunt, R. M.; Brown, S. P. *J. Phys. Chem. A* **2010**, *114*, 10435−10442.
(74) Brouwer, D. H. *J. Magn. Reson.* **2008**, *194*, 136−146.
(75) Brouver, D. H. *J. Am. Chem. Soc.* **2008**, *130*, 6306−6307.
(76) Martineau, C.; Fayon, F.; Legein, C.; Buzaré, J.-Y.; Body, M.; Massiot, D.; Goutenoire, F. *Dalton Trans.* **2008**, 6150−6158.
(77) Martineau, C.; Fayon, F.; Suchomel, M. R.; Allix, M.; Massiot, D.; Taulelle, F. *Inorg. Chem.* **2011**, *50*, 2644−2653.
(78) Gervais, C.; Dupree, R.; Pike, K. J.; Bonhomme, C.; Profeta, M.; Pickard, C. J.; Mauri, F. *J. Phys. Chem. A* **2005**, *109*, 6960−6969.
(79) Pourpoint, F.; Kolassiba, A.; Gervais, C.; Azais, T.; Bonhomme-Coury, L.; Bonhomme, C.; Mauri, F. *Chem. Mater.* **2007**, *19*, 6367−6369.
(80) Gervais, C.; Laurencin, D.; Wong, A.; Pourpoint, F.; Labram, J.; Woodward, B.; Howes, A. P.; Pike, K. J.; Dupree, R.; Mauri, F.; Bonhomme, C.; Smith, M. E. *Chem. Phys. Lett.* **2008**, *464*, 42−48.
(81) Cahill, L. S.; Hanna, J. V.; Wong, A.; Freitas, J. C. C.; Yates, J. R.; Harris, R. K.; Smith, M. E. *Chem.—Eur. J.* **2009**, *15*, 9785−9798.
(82) Pallister, P. J.; Moudrakovski, I. L.; Ripmeester, J. A. *Phys. Chem. Chem. Phys.* **2009**, *11*, 11487−11500.
(83) Widdifield, C. M.; Bryce, D. L. *J. Phys. Chem. A* **2010**, *114*, 2102−2116.
(84) Griffin, J. M.; Yates, J. R.; Berry, A. J.; Wimperis, S.; Ashbrook, S. E. *J. Am. Chem. Soc.* **2010**, *132*, 15651−15660.
(85) Charpentier, T. *Solid State NMR* **2011**, *40*, 1−20.
(86) Menconi, G.; Tozer, D. J. *Chem. Phys. Lett.* **2002**, *360*, 38−46.
(87) Charpentier, T.; Ispas, S.; Profeta, M.; Mauri, F.; Pickard, C. J. *J Phys. Chem. B* **2004**, *108*, 4147−416.
(88) Schoonman, J.; Oversluizen, G.; Wapernaar, K. E. D. *Solid State Ionics* **1980**, *1*, 211−221.
(89) Réau, J.-M.; Lucat, C.; Portier, J.; Hagenmuller, P.; Cot, L.; Vilminot, S. *Mater. Res. Bull.* **1978**, *13*, 877−882.
(90) Lucat, C.; Sorbe, P.; Portier, J.; Hagenmuller, P.; Grannec, J. *Mater. Res. Bull.* **1977**, *12*, 145−150.
(91) Li, C.; Quan, Z.; Yang, J.; Yang, P.; Lin, J. *Inorg. Chem.* **2007**, *46*, 6329−6337.